Final state interactions in $^2H(\gamma,pp\pi^-)$ near the $\Delta(1232)$ resonance

M. A. Quraan, E. D. Hackett, E. Korkmaz,* W. J. McDonald, A. K. Opper,†
and N. L. Rodning
Centre for Subatomic Research, University of Alberta, Edmonton, Alberta, Canada T6G 2N5

G. Feldman,‡ N. R. Kolb, G. V. O'Rielly,* R. E. Pywell, and D. M. Skopik
Saskatchewan Accelerator Laboratory, University of Saskatchewan, Saskatoon, Saskatchewan, Canada S7N 5C6

(Received 10 November 1997)

The $^2H(\gamma,pp\pi^-)$ reaction cross section has been measured in the energy range 220 MeV$\leqslant E_\gamma \leqslant$280 MeV at the Saskatchewan Accelerator Laboratory using the Saskatchewan-Alberta Large Acceptance Detector. This is the first reported measurement of the $\gamma^2H\rightarrow pp\pi^-$ cross section covering a wide range of phase space in an attempt to study final state interactions. The cross section for this reaction is compared to the calculation of Blomqvist and Laget with various contributions from final state interactions. Blomqvist and Laget's theory is successful in describing the shapes of the distributions, as well as the overall magnitude of the cross section. The different final state interactions have an overall effect of 10%–15% on the single differential cross section, with the calculation that includes the Δ-N interaction having the best agreement with the data. [S0556-2813(98)00304-5]

PACS number(s): 21.45.+v, 13.75.Cs, 25.20.Dc, 25.20.Lj

I. INTRODUCTION

Previous $\gamma^2H\rightarrow pp\pi^-$ experiments focused on kinematic conditions where the spectator model, which is independent of the nuclear medium, is expected to be valid [1]. In contrast, our experiment has emphasized measuring this reaction away from these quasifree kinematic conditions in order to examine the details of how the nuclear medium actually modifies this basic interaction. These final state interactions (FSI's) have been examined in many reaction processes; however, the $\gamma^2H\rightarrow pp\pi^-$ reaction offers a unique system.

Of the different FSI's that may occur in this reaction, the Δ-N interaction is the least well understood. The experimental difficulty in studying this interaction arises from the fact that the Δ is an unstable particle with a very short lifetime (width, Γ=115 MeV; mean life, $\tau=6\times10^{-24}$ s). The short lifetime introduces complications in the theoretical description as well. A complete calculation would require a solution to the coupled channel problem for $NN\rightarrow N\Delta$. This is a challenging job, and only approximate solutions have been attempted. The amount of data constraining the calculations is limited and confined to specific reactions [2–4]. There is a definite need for both complete theoretical calculations of the Δ-N interaction as well as experimental data from various reaction mechanisms to allow for definite conclusions and consistency checks.

To investigate FSI's in $\gamma^2H\rightarrow pp\pi^-$, theoretical calculations were carried out by Blomqvist and Laget by expanding the transition amplitude in terms of a few relevant processes [5–7]. The calculations include different ingredients of FSI's (π-N rescattering, N-N rescattering, and the Δ-N interaction) and the final state kinematics may be chosen to focus on the FSI of interest. This method has been quite successful in reproducing a large body of experimental data. The data used in these comparisons, however, were restricted to small regions of phase space, as only small acceptance detectors were used [2,3]. In this paper, we expand such comparisons to cover nearly 4π acceptance.

The experiment described here was performed at the Saskatchewan Accelerator Laboratory (SAL). Outgoing charged particles were detected using the Saskatchewan-Alberta Large Acceptance Detector (SALAD). The high duty factor SAL machine and SALAD are described briefly below; a detailed description may be found elsewhere [8–10]. This is the first successful measurement of the $\gamma^2H\rightarrow pp\pi^-$ cross section with 4π acceptance. A similar measurement was attempted at Mainz a few years ago and failed to obtain results consistent with Blomqvist and Laget's calculations [11]. SALAD has been a useful device in the investigation of other reactions as well. Since it has been stationed at SAL, several experiments have been performed on ^2H, ^3He, ^4He, and ^{12}C targets. Most of the data obtained have been analyzed and published [12–18].

II. EXPERIMENTAL SETUP

This experiment was performed at the Saskatchewan Accelerator Laboratory using the Saskatchewan-Alberta Large Acceptance Detector. SAL provides a high duty factor electron beam, produced by a linear accelerator and a pulse stretcher ring, which may be used in conjunction with a 62-channel photon tagging system [19]. The linac was tuned to obtain the maximum electron energy possible at the time, resulting in 290 MeV and 284 MeV, for two different sets of measurements, with an average duty factor of 44%. The beam was then passed through a 115-μm-thick aluminum radiator, resulting in a photon beam with a flux of 3.5 MHz

*Present address: Physics Department, University of Northern British Columbia, Prince George, British Columbia, Canada V2N 4Z9.

†Present address: Physics Department, University of Ohio, Athens, Ohio 45701.

‡Present address: Department of Physics, The George Washington University, Washington, D.C. 20052.

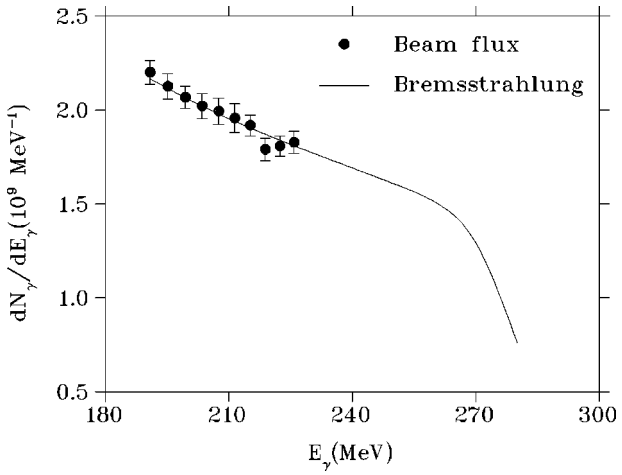

FIG. 1. Bremsstrahlung photon energy distribution (solid curve) fitted to the photon beam flux computed from the tagger counting rates (circles).

in the range 220 MeV$\leqslant E_\gamma \leqslant$280 MeV. While SAL is capable of providing a higher flux, the rate was kept low enough to ensure a clean tracking of particles in the wire chambers.

The system was adjusted to allow the tagging of photons in the maximum energy range possible. This results in the tagging of photons in the energy range 187–229 MeV, with the upper limit dictated by the magnet geometry. In this experiment, only events that result in three signals in the SALAD calorimeter were analyzed. In most cases, such events result from photons above that of the tagged range. Since the kinematics of these events are overdetermined, the photon energy was determined from the kinematics. The tagger was useful, however, in the photon flux determination, as the photon flux in the tagged region was extrapolated using a bremsstrahlung distribution to determine the flux in the untagged region. Figure 1 shows this extrapolation at the lower electron energy.

The photon beam was collimated using two 12.6-cm-long lead collimators of 1.5 and 2.0 cm diameter. The positions of these two collimators (perpendicular to the beam line) were adjusted under computer control, and several tests were performed to fine-tune their positions by monitoring the increase of the background rate in SALAD as the collimators' positions were varied. A lead wall, 9 cm thick, was placed between the second collimator and SALAD to provide shielding from backgrounds associated with the beam dump. A third collimator was fitted in the lead wall, with a radius of 3.0 cm which was large enough so that the primary collimated beam was not affected. To further reduce the background, a 26-cm-long, 2.32-cm-thick removable lead shielding of 12.1 cm diameter was mounted at the upstream end of SALAD as shown in Fig. 2.

Tagging efficiency measurements were carried out using a lead-glass detector (located behind the downstream end of SALAD) with a cross sectional area bigger than that of the collimated beam. These measurements were carried out at a much lower photon flux than production runs to avoid pileup in the lead-glass detector. Tests were performed which show that, in the range of interest, the tagging efficiency is flux independent. After tagging efficiency measurements were performed, the lead-glass detector was remotely moved away

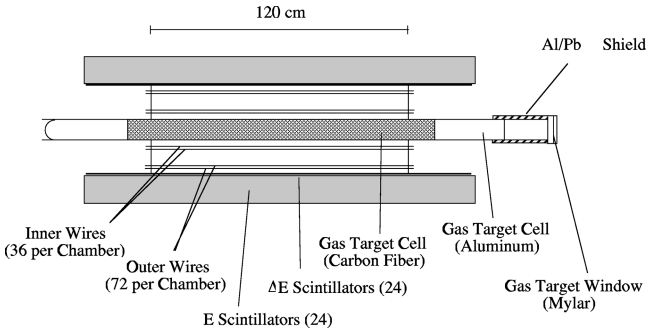

FIG. 2. Side view of the Saskatchewan-Alberta Large Acceptance Detector (SALAD).

from the beam line. The tagging efficiency (summed over the 62 channels) averaged to 49% at the lower electron energy and 56% at the higher electron energy. The total number of photons in the range 220 MeV$\leqslant E_\gamma \leqslant$280 MeV was determined to be 3.6×10^{11} to within 4%.

The target in this experiment consisted of a pressurized cylinder with an overall length of 237 cm and an inner radius of 5.05 cm. The main portion of the target is made up of a 208.3-cm-long Mylar-lined carbon fiber tubing. The cylinder was filled with deuterium gas at room temperature with an initial absolute pressure of 70.8 kPa. Small amounts of leakage caused the pressure to drop off to 65.0 kPa atmospheres at the end of the 1-week-long production run. Both pressure and temperature were monitored throughout the experiment, and a weighted average was calculated for the uncertainty in the target density, resulting in a systematic uncertainty of 4%. The target was mounted in the center of SALAD, with its axis parallel to that of SALAD.

The detector system (SALAD) consists of two inner wire chambers and two outer wire chambers operating in the self-quenching streamer mode for particle tracking, surrounded by a set of 24 ΔE-E plastic scintillators for energy measurement and particle identification (Fig. 2). The inner chambers contain 36 wires each, whereas the outer chambers contain 72 wires each. The finite spacing between the wires limits the ϕ resolution to about $\sigma_\phi = 2.6°$. The z-position resolution of the wires results in a resolution in θ that is θ dependent, varying from $\sim 0.2°$ at the smallest (and largest) θ-angle acceptance (of 15° and 165°) to $\sim 5°$ at normal incidence. The walls of the wire chambers are made up of low density polyurethane foam to reduce the energy loss of passing particles and allow them to be detected in the calorimeter, while avoiding dead zones that would result from the use of supporting rods. The ΔE scintillators have a length of 180.3 cm and a thickness of 0.32 cm, while the E scintillators have a length of 182.9 cm and a thickness of 12.75 cm. The energy resolution of the scintillators was determined from overdetermined kinematics obtained from $^3He(\gamma,pd)$, $^2H(\gamma,p)n$, and p-p elastic scattering experiments [12,10]. Cosmic ray data obtained in conjunction with these data sets determined the average stopping power for cosmic rays tracked through SALAD.

III. DATA ANALYSIS

Only overdetermined events were analyzed to reduce the background and allow an accurate determination of the kine-

matics. At least two calorimeter signals exceeding a set threshold were therefore required to occur in coincidence with the tagger for a valid trigger. As most events with three calorimeter signals will result from photons with energies above that of the tagger range, the requirement for the presence of a tagger signal was dropped in this case.

The combined effect of low particle energies and relatively high detector thresholds results in drastically reducing the number of detected $^2\mathrm{H}(\gamma,pp\pi^-)$ events. The highest photon energy was ~290 MeV. Since a pion is formed, 139.6 MeV are lost, and the remaining ~150 MeV are distributed as kinetic energy among the three outgoing particles. In this energy region, the quasifree process is dominant and one of the protons is a spectator which does not share this energy. This proton will likely lose its energy before it gets to the ΔE scintillators; thus the two-track $\gamma^2\mathrm{H}\rightarrow pp\pi^-$ events will typically result from quasifree processes. These events are mixed with a large background due to $\gamma\rightarrow e^+e^-$ events which produce two coincident hits in the SALAD calorimeter. Analysis of the two-calorimeter trigger events shows that these events are mostly background; therefore, only three-calorimeter trigger events were selected as $^2\mathrm{H}(\gamma,pp\pi^-)$ candidate events. While this greatly reduces the size of the data set, and thus reduces the effective efficiency of the event selection, the events discriminated against tend to be those generated by the quasifree process. The selected data set has increased sensitivity to the more interesting FSI's.

An additional concern arises from the strong absorption of pions in the SALAD calorimeter. The strong interaction of the absorbed pions with the nucleus occurs on a time scale that is much shorter than that of the signal processing electronics (10^{-25} s for pion absorption compared with 10^{-8} s for the signal gating time in the electronics). If a pion stops in the E scintillator and is absorbed, the processed signal is a sum of the pion's kinetic energy and the energy deposited by the particles released in the process [20]. The energy deposited in the E scintillator may thus be larger than the pion kinetic energy, and therefore was not used in the analysis. Furthermore, the pion energy shift results in a fair amount of mixing between pions and protons on a stopping power histogram (Fig. 3). It was determined that about 20% of the pions will have a particle ID value (pid, obtained by linearizing the stopping power plot [14]) that corresponds to a proton as a result of this process. Many of the $^2\mathrm{H}(\gamma,pp\pi^-)$ events will be interpreted as three-proton events. In such a case, stopping power information was disregarded. Since the kinematics of these events are overdetermined, permutations were made over the possible particle types (p, π), and the permutation best satisfying the kinematics was chosen as the correct one. This resulted in lowering the systematic uncertainty due to particle misidentification to 1%. Figure 3 shows a stopping power histogram for the $^2\mathrm{H}(\gamma,pp\pi^-)$ events, as well as a linearized stopping power (pid) histogram.

A kinematic fitting program was used to analyze the data. A χ^2 distribution was defined by

$$\chi^2=\frac{1}{N}\sum_i\left(\frac{v_i^m-v_i^f}{\sigma_i}\right)^2, \tag{1}$$

where v_i^m is the ith measured variable, v_i^f is the ith variable

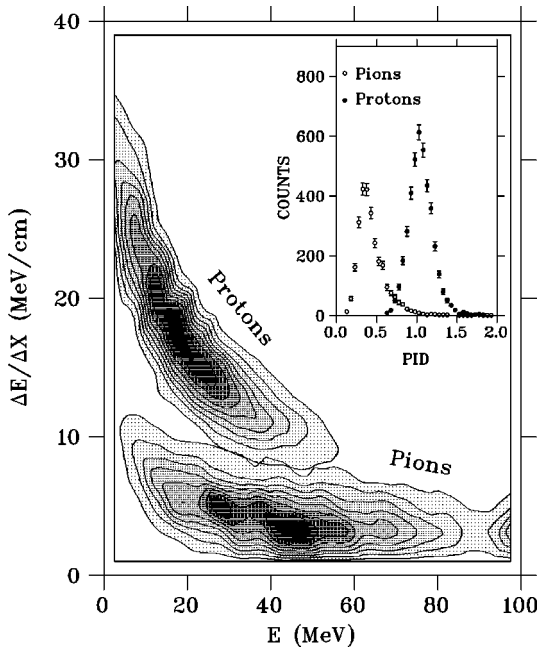

FIG. 3. Stopping power versus energy for $^2\mathrm{H}(\gamma,pp\pi^-)$ events. The figure in the top right corner is a linearized stopping power (pid) histogram.

determined from the fit, σ_i is the detector's resolution for that variable, and N is the number of variables in the fit. Results from the kinematic fit were compared to analytic solutions. A fit has two advantages over an analytic solution: First, a χ^2 distribution may be used to characterize and eliminate the background, and second, a fit allows a more accurate determination of the unknown kinematic variables as well as the measured quantities. In this analysis, only two types of events were accepted as $^2\mathrm{H}(\gamma,pp\pi^-)$ candidate events: those for which measurements of θ, ϕ, and ΔE (energy deposited in the ΔE scintillator) have been made for all three tracks and where an E signal (energy deposited in the E scintillators) exists for one or both of the proton tracks (the pion energy was not used as it may be obscured due to the absorption process). These quantities were used as inputs to the kinematic fit together with their respective weights, calculated from the angular and energy resolutions discussed above. The constraints of the fit were minimized by varying the measured variables within their respective weights. Once the measured variables were constrained, the unknown kinematic variables (the energy deposited by the pion in the E scintillators, the photon energy, and the energy deposited by a proton in the E scintillators if not measured) were calculated. A kinematic χ^2 value was calculated for each event. Figure 4 shows the χ^2 distribution for the $^2\mathrm{H}(\gamma,pp\pi^-)$ events. A cut was imposed on this distribution as shown in the figure to eliminate the background. The solid histogram is a Monte Carlo simulation of SALAD (to be described below). A slight disagreement may be seen as a result of the uncertainty in the detector resolution.

The Monte Carlo simulation generates events according to a three-body phase space distribution, taking into account the spatial distribution of the photon beam. For untagged events, the Monte Carlo simulation uses a bremsstrahlung distribution calculated at the proper electron energy. Each particle was tracked through the various layers of the detec-

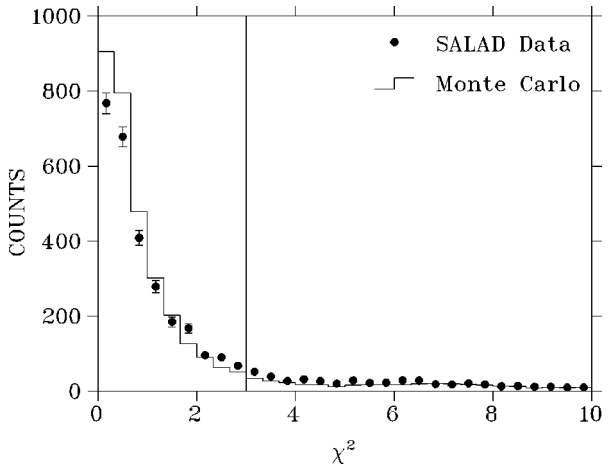

FIG. 4. Kinematic χ^2 distribution for $^2H(\gamma,pp\pi^-)$ events. A cut is imposed on this distribution at $\chi^2=3$. The solid histogram is a Monte Carlo simulation.

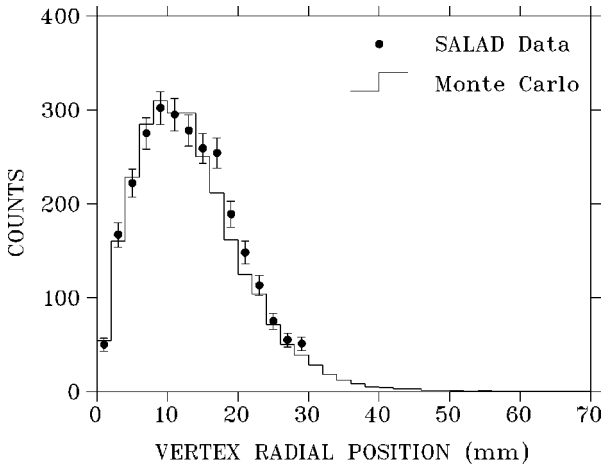

FIG. 5. Radial position of the vertex for $^2H(\gamma,pp\pi^-)$ events. The solid histogram is a Monte Carlo simulation.

tor, and the energy deposited in each layer was calculated. As each particle was tracked in the wire chambers, the wire chamber cells intersected by the track were determined, as well as the z position of the hit on the wire. This z position was smeared out to take into account the wire chamber resolutions, as measured using an ^{55}Fe collimated source. The analog-to-digital converter (ADC) values at each end of the wire were then calculated. The wires' efficiencies were also calculated for each of the 216 wires and incorporated into the Monte Carlo simulation. Events from $^{12}C(\gamma,pp)$ were used for this purpose, where the efficiency of a wire cell was determined by the frequency of the occurrence of a signal in that wire cell when cells in each of the other three chambers register a hit. The overall systematic uncertainty due to the wire chamber calibrations and efficiencies was less than 5%.

Once the ADC values of the wires were determined, the particle tracking proceeded to the calorimeter and the energy deposited in the ΔE and E scintillators was determined. The light output was then calculated by reversing the light correction process [21]. This requires knowledge of the attenuation lengths, which were calculated separately for each ΔE and E scintillator from overdetermined kinematics for events of other reactions. The resulting light outputs were smeared out to account for the ΔE and E energy resolutions mentioned above, and the ADC values were calculated for the upstream and downstream ends of each scintillator. Since this calculation is sensitive to small uncertainties in the material thickness and density in the walls of SALAD, a systematic uncertainty of 5% was assigned to the particle energies.

Other corrections were included in the Monte Carlo simulation, including proton reaction losses and pion absorption. The GEANT Monte Carlo simulation package GHEISHA was used to simulate the process of reaction losses. This process has a small contribution in our energy range. The number of protons that deposit a different amount of energy than expected due to nuclear interactions was less than 0.5%. The pion absorption process, on the other hand, is difficult to simulate exactly. To account for this process an approximate solution was chosen. The shift in the observed pion energy was determined from the data, by taking the difference between the actual energy deposited in the E scintillator and that determined from the kinematic fit. This distribution was used as an input to the Monte Carlo simulation, and pion energies were shifted according to this probability distribution.

A full account of the pion decay process was also included in the Monte Carlo simulation. The lifetime of the pion was taken from the pion decay probability distribution and the decay length was determined. For decays occurring inside the target or the wire chambers, the muon's emission angle and energy were selected consistent with the kinematics of the decay process, and the muon was tracked instead of the pion. The wire chamber hits were then modified to account for the muon track and the resulting hits were used to attempt to reconstruct a track, assuming it was due to a single particle. Since this was not the case, a track is unlikely to be successfully reconstructed, the event falls in the two-track category, and was thus discarded. If a track was successfully reconstructed, the θ and ϕ angles were likely to be off the values expected from the $^2H(\gamma,pp\pi^-)$ kinematics, resulting in a large value for χ^2 which would fail the χ^2 cut.

By simulating Monte Carlo events with and without pion decay, it was determined that 6% of the events are lost due to this process. It is worth noting at this point that since the pion's energy was not used, muons that decay outside the wire chambers need not be tracked.

The simulated events were then tested to determine whether they satisfy the experimental trigger. Thresholds were determined for each ΔE and E scintillator separately from the raw ADC spectra and used as input to the Monte Carlo. Monte Carlo events that do not satisfy the threshold or do not fall within the detector's acceptance had their ADC values set to zero. Events that satisfy this threshold were written to disk. The Monte Carlo events were then read by the same analysis code used to analyze the actual experimental data, using the same calibration parameters (energy loss tables, light correction tables, etc.). This ensures that any deviation of the data from the Monte Carlo simulation is due to dynamical physical effects. In addition, the Monte Carlo simulation allows for a large number of variables to be compared to the data at any step of the analysis, starting with the ADC values, and ending with kinematic quantities. This allows us to demonstrate our understanding of the detector, and provides additional confidence in the calculation of the

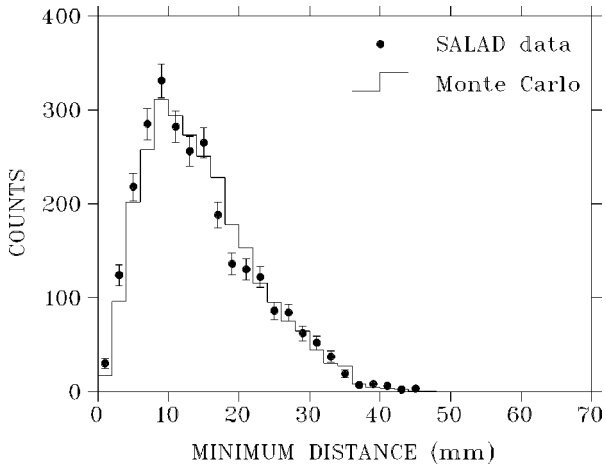

FIG. 6. Average minimum distance between outgoing tracks for ^{2}H($\gamma,pp\pi^-$) events. The solid histogram is a Monte Carlo simulation.

efficiency of the SALAD detector.

Figure 5 shows the radial position of the vertex distribution for the ^{2}H($\gamma,pp\pi^-$) events. The distribution matches that predicted by the SALAD Monte Carlo simulation. A cut was imposed on this distribution to eliminate the background as shown in the figure. No cuts were imposed on the distribution of the minimum distance between outgoing tracks (mindis). As may be seen from Fig. 6, good agreement with the simulation is obtained, and no background is evident.

IV. RESULTS AND DISCUSSION

When a Δ is produced in the intermediate state, the three particles involved (photon, proton, and Δ) lie in a single plane as required by momentum conservation. Similarly, the particles involved in the Δ decay process lie in one plane. This results in two planes with the track defining the direction of the Δ being common to both, as shown in Fig. 7. With no dynamical physical processes present, the two planes have a random orientation with respect to each other, with the direction of the Δ defining the axis of rotation. In a coordinate system where the direction of the Δ defines the z axis, the angle between the two planes is the azimuthal angle of the pion, ϕ_π.

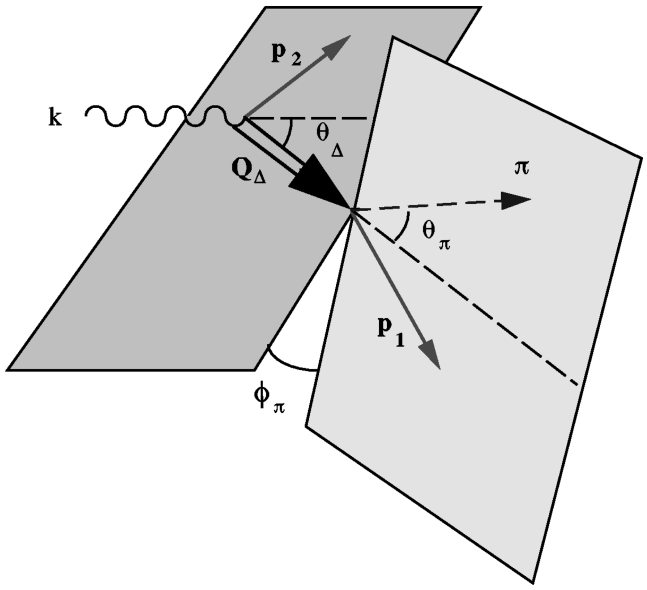

FIG. 7. A schematic diagram of the ^{2}H($\gamma,pp\pi^-$) reaction, showing the intermediate process resulting in the creation of the $\Delta(1232)$ resonance and its subsequent decay. The definition of the kinematic variables used to calculate the cross section is also shown in the plot.

For three-body final states, six variables (including the incident energy) are needed to uniquely identify the kinematics of the event. However, for an unpolarized beam and target, one of these variables is a trivial overall azimuthal rotation which need not be considered, and so the cross section may be described by a set of five variables. In this experiment, the dynamics of the Δ are of particular interest, and so the variables chosen are those that best describe the reaction in terms of the intermediate Δ-N state. The photon energy E_γ, the p-π invariant mass Q_Δ, the Δ scattering angle θ_Δ, and the pion scattering angles θ_π and ϕ_π were used (see Fig. 7). The Δ scattering angle is boosted to the γ-^{2}H center-of-mass frame and labeled $\theta_\Delta^{\text{c.m.}}$. The pion's scattering angles were boosted to the Δ rest frame and labeled θ_π^* and ϕ_π^*. In terms of these five variables, the fivefold differential cross section may be written as

$$\frac{d^5\sigma}{dE_\gamma dQ_\Delta d\cos\theta_\Delta^{\text{c.m.}} d\cos\theta_\pi^* d\phi_\pi^*}(E_\gamma,Q_\Delta,\cos\theta_\Delta^{\text{c.m.}},\cos\theta_\pi^*,\phi_\pi^*)=\frac{\left(\frac{Y(E_\gamma,Q_\Delta,\cos\theta_\Delta^{\text{c.m.}},\cos\theta_\pi^*,\phi_\pi^*)}{\Delta E_\gamma \Delta Q_\Delta \Delta\cos\theta_\Delta^{\text{c.m.}} \Delta\cos\theta_\pi^* \Delta\phi_\pi^*}\right)}{N_\gamma(E_\gamma)\times N_t\times\varepsilon(E_\gamma,Q_\Delta,\cos\theta_\Delta^{\text{c.m.}},\cos\theta_\pi^*,\phi_\pi^*)}. \quad (2)$$

Defining a set of variables q_i as

$$\{q_i\}=\{E_\gamma,Q_\Delta,\cos\theta_\Delta^{\text{c.m.}},\cos\theta_\pi^*,\phi_\pi^*\}, \quad (3)$$

the numerator on the right-hand side of Eq. (2) may be written as $Y(\{q_i\})/\Pi_i\Delta q_i$. This factor is the experimental yield in a given bin divided by the bin width, $N_\gamma(E_\gamma)$ is the photon flux, N_t is the number of target nuclei per unit area, and $\varepsilon(\{q_i\})$ is the efficiency of the detector.

The geometrical acceptance of SALAD is dependent on the position of the target nuclei along the z axis, being maximum at the center and dropping down towards either end. On the other hand, the geometrical acceptance is different for different events originating from the same position along the z axis due to the coincidence requirement, and depends on

the direction and energies of the outgoing particles. The intrinsic efficiency of the detector is also strongly dependent on the kinematics of the event, as the energy deposited in each layer of the detector is strongly dependent on both the particle's energy and emission angle. Whether an event will cause a three-calorimeter trigger requires knowledge of the kinematics of all three outgoing particles so that the energy loss in the walls of SALAD may be calculated for each track separately to determine whether each particle will have enough energy to cause a trigger. One has, therefore, to determine whether the event generated will be detected for each event separately. An efficiency may be defined as

$$\varepsilon(E_\gamma, Q_\Delta, \cos\theta_\Delta^{\text{c.m.}}, \cos\theta_\pi^*, \phi_\pi^*) = \frac{N_{\text{det}}(E_\gamma, Q_\Delta, \cos\theta_\Delta^{\text{c.m.}}, \cos\theta_\pi^*, \phi_\pi^*)}{N_{\text{gen}}(E_\gamma, Q_\Delta, \cos\theta_\Delta^{\text{c.m.}}, \cos\theta_\pi^*, \phi_\pi^*)}, \tag{4}$$

where $N_{\text{gen}}(\{q_i\})$ is the number of Monte Carlo–generated events, and $N_{\text{det}}(\{q_i\})$ is the number of detected (and accepted) events.

In addition to the geometric acceptance and intrinsic efficiency of the detector, the factor $\varepsilon(\{q_i\})$ takes into account all the cuts applied in the analysis, including cuts aimed at eliminating the background. The efficiency factor thus accounts for any good events lost due to the cuts. The Monte Carlo simulation, however, does not account for background events that may have survived the cuts. This contamination is estimated to be less than 2%, as verified by the good agreement between the data and the Monte Carlo simulation for the various distributions. In particular, the mindis distribution of Fig. 6 has no cuts imposed on it, but no events are seen with a mindis value greater than 45 mm. Similarly, the pid spectrum of Fig. 3 shows no evidence of an electron contamination.

Calculation of the efficiency factor was quite cumbersome. The number of generated and detected events was required to be large enough so that the statistical uncertainties in the determination of the efficiency factor does not impose a limit on the accuracy of the cross section. In this experiment, a threefold coincidence was required. The highly selective nature of the analysis resulted in a very low efficiency (detected events/generated events). Here 45×10^6 Monte Carlo events had to be generated and analyzed, and the efficiency was determined in terms of the five variables, binned the same as the data.

The fivefold differential cross section calculated in Eq. (2) was binned in 10 bins for each variable resulting in 10^5 bins. To calculate a single differential cross section, a summation is required over the other four variables. For example, to calculate the cross section as a function of the variable q_k we have

$$\frac{d\sigma}{dq_k}(q_k) = \sum_{i\neq k}\left(\frac{d^5\sigma}{\Pi_j dq_j}(\{q_i\})\prod_{i\neq k}\Delta q_i\right). \tag{5}$$

The resulting cross sections in terms of the five variables $\{q_i\}$ are shown in Fig. 8. The error bars are a combination of the statistical uncertainties in the data as well as the systematic and statistical uncertainties in the tagging efficiency

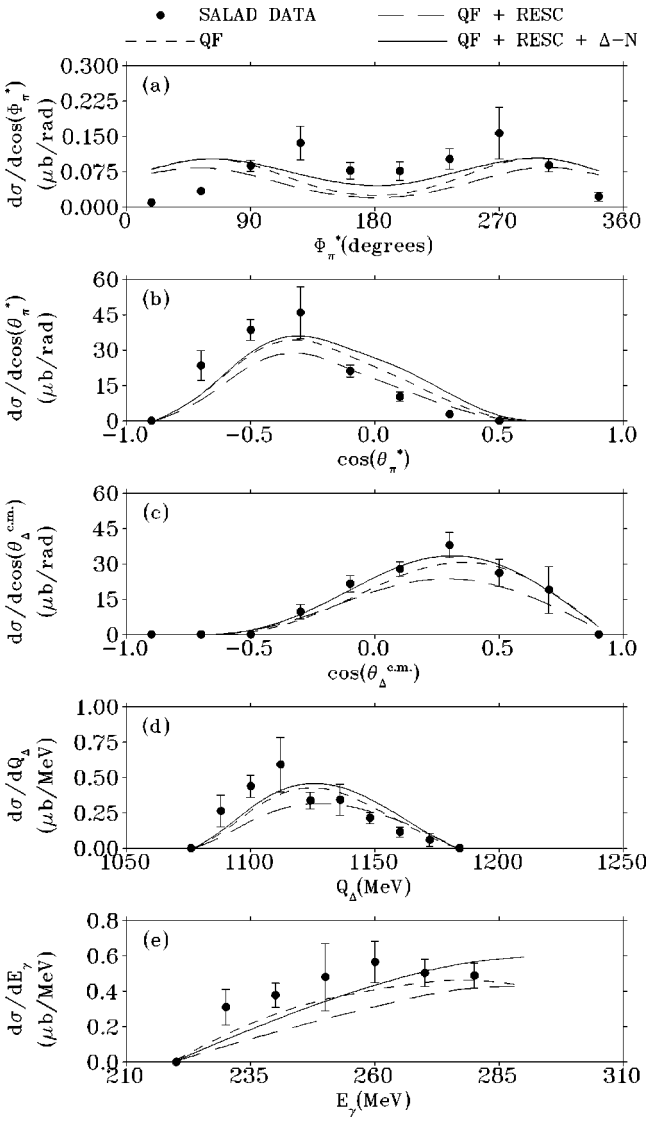

FIG. 8. Single differential cross sections for ^{2}H($\gamma,pp\pi^-$) in terms of the π (a) azimuthal angle ϕ_π^* and (b) scattering angle θ_π^*, both calculated in the Δ rest frame where the direction of the Δ defines the z axis, (c) the Δ scattering angle θ_Δ^* calculated in the γ-^{2}H center-of-mass frame, (d) the p-π^- invariant mass Q_Δ, and (e) the beam energy E_γ. The curves represent the theoretical calculations of Blomqvist and Laget, and are corrected for the efficiency of SALAD. The short-dashed curve includes only quasifree Feynman diagrams, and the long-dashed curve includes rescattering diagrams, whereas the solid curve includes Δ-N diagrams as well. A systematic uncertainty of 9% is not included in the error bars.

measurements, but do not include systematic uncertainties from the other sources mentioned above. If added in quadrature, these sources result in an overall additional systematic uncertainty of 9%. The shapes of these distributions are a convolution of both the actual physical processes (both phase space and dynamics), as well as the geometrical acceptance of SALAD and the cuts imposed in the analysis. For example, if the cross section is plotted in terms of the pion's scattering angle in the laboratory frame, a certain range of forward and backward angles would be identically zero due to the acceptance of SALAD. This would result in a nontrivial effect on the shapes of the cross section when plotted

TABLE I. Total cross section for $^2H(\gamma,pp\pi^-)$ calculated at the center of the photon beam energy range (220 MeV$\leq E_\gamma \leq$280 MeV). Also listed are the results of Blomqvist and Laget's calculations including different FSI's. A systematic uncertainty of 9% is not included in the error quoted in the table.

Description	$\sigma(\mu b)$
This work	141.9 ± 1.5
Quasifree	127.0
Quasifree+ rescattering	102.1
Quasifree+rescattering+Δ-N interaction	141.0

in terms of other variables, as the measured variables are effectively integrated over. This makes it hard to draw any significant conclusions directly from the figures. A comparison to an actual model is required, in which the above-mentioned effects are taken into account.

The particular shape of the ϕ_π^* distribution [Fig. 8(a)] is a good example of how the cuts imposed in the analysis may affect the shapes of these distributions. A strong dip is noticed at $\phi_\pi^*=0°/360°$ and 180°. These values of ϕ_π^* correspond to one of the decay products going out at the same azimuthal angle (in the laboratory frame) as the spectator nucleon, thus hitting the same scintillator bar. Such events are excluded from the analysis as energies deposited in the ΔE and E scintillators are not independently available for each particle. Figures 8(b) and 8(c) show the single differential cross section in terms of the variables $\cos(\theta_\pi)$ and $\cos(\theta_\Delta)$, respectively. The regions where the cross section goes to zero are inaccessible due to the acceptance of SALAD. Although the inaccessible regions in the scattering angle distribution are expected to be the same at forward and backward angles due to the symmetry of the detector, the particular choice of coordinate system and reference frame results in shifting this symmetry.

The cross section as a function of the p-π invariant mass and the photon energy are shown in Figs. 8(d) and 8(e), respectively. The E_γ distribution has the expected shape, showing a rise as a result of the production of the Δ resonance. The Q_Δ distribution has the expected shape as well. The production of the Δ resonance results in the initial steep rise of the cross section. Because of the maximum photon energy, however, the amount of phase space accessible to the Δ decreases as higher photon energies are not possible, and the distribution decreases monotonically until it hits zero at the point where the highest photon energy has been reached. Table I lists the total cross section obtained by integrating the $d\sigma/dE_\gamma$ distribution over the measured range of photon energy.

The only theoretical calculation available to us is that of Blomqvist and Laget. The curves in Fig. 8 show the results of this calculation including different FSI's. The short-dashed curve includes the quasifree diagram only, and the long-dashed curve includes rescattering effects (both N-N and π-N rescattering), whereas the solid curve includes the short-range Δ-N interaction as well. The theoretical calculation was binned in the same 10^5 bins as the data and then integrated in the same manner. The acceptance of SALAD was applied to the theoretical calculation by setting the theoretical calculation to zero in any bin for which the efficiency calculation yields a zero value in the corresponding bin. As may be seen from the figures, the theoretical calculations describe the data reasonably well except for the ϕ_π^* distribution. In addition the overall normalizations are in good agreement, particularly with the calculation that includes both rescattering effects and the Δ-N interaction, as may be seen from Table I.

We conclude from these comparisons that the overall effect of the FSI's on the single differential cross section is about 10%–15%. This is a small effect, which is not particularly surprising, since we are looking at a single differential cross section (integrated over the other four variables). When integrating over many variables, any interesting effects that may be present in particular regions of phase space as a result of a strong contribution from a particular diagram will be washed out in the integration process. The best method to single out a particular diagram is to focus on a specific region of phase space where that diagram makes a strong contribution. To do this, we have extracted the two-dimensional cross section with respect to the Δ mass and each of the other four variables and compared that to Blomqvist and Laget's calculation. In each case our statistical uncertainties are bigger than the variations between the different ingredients of the theoretical calculation. The comparison of the single differential cross section confirms, however, that there are no strong effects of FSI's that contribute in a wide range of phase space to the extent that they prevail when a single differential cross section is calculated.

V. CONCLUSIONS

This is the first measurement of the $\gamma^2H \rightarrow pp\pi^-$ cross section covering a wide range of phase space which successfully constrains the FSI's including the short-range Δ-N interaction. Blomqvist and Laget's theory is quite successful in describing the shapes of the distributions, as well as the overall magnitude of the cross section. The different FSI's have an overall effect of 10%–15% on the single differential cross section, with the calculation that includes the Δ-N interaction having the best agreement compared to the data.

Explicit comparisons to other experiments are hard to make in this case. Most pre-existing data sets were obtained with small acceptance detectors and are thus confined to a very limited range of phase space. Our data, on the other hand, are spread over a 4π acceptance with limited statistics, and the shape of our cross section in terms of the different variables is highly dependent on the geometrical acceptance of SALAD and the cuts imposed in the analysis. It should be noted, however, that the good agreement with Blomqvist and Laget's theory implies a good agreement with other experiments as well, as Blomqvist and Laget's theory has been compared to the various experimental data available [2,3].

We were unable, however, to single out the effects of the different diagrams. This is a result of the limited statistics achieved in this experiment. In order to do such a detailed comparison, one needs to focus on the particular range of phase space in which a certain diagram (FSI) has a strong contribution. This requires looking at a multidifferential cross section, which in turn requires high statistics.

ACKNOWLEDGMENTS

The authors would like to thank J. M. Laget for providing the theoretical calculations and F. C. Khanna for many useful discussions. This work was supported by the Natural Sciences and Engineering Research Council of Canada.

[1] P. Benz *et al.*, Nucl. Phys. **B65**, 158 (1973).
[2] P. E. Argan *et al.*, Nucl. Phys. **A296**, 373 (1978).
[3] P. E. Argan *et al.*, Phys. Rev. Lett. **41**, 86 (1978).
[4] Erasmo Ferreira and H. G. Dosch, Phys. Rev. C **40**, 1750 (1989).
[5] I. Blomqvist and J. M. Laget, Nucl. Phys. **A280**, 405 (1977).
[6] J. M. Laget, Nucl. Phys. **A296**, 388 (1978).
[7] J. M. Laget, Phys. Rep. **69**, 1 (1981).
[8] L. A. Dallin, in Proceedings of the 1989 IEEE Part. Acc. Conference, 1989 (unpublished), p. 1.
[9] E. B. Cairns *et al.*, Nucl. Instrum. Methods Phys. Res. A **321**, 109 (1992).
[10] P. P. Langill, M.Sc. thesis, University of Alberta, 1989.
[11] S. Kerhoas, Ph.D. thesis, Université de Paris Sud, 1993.
[12] N. R. Kolb *et al.*, Phys. Rev. C **49**, 2586 (1994).
[13] N. R. Kolb *et al.*, Phys. Rev. C **54**, 2175 (1996).
[14] E. D. Hackett *et al.*, Phys. Rev. C **53**, R1047 (1996).
[15] E. D. Hackett, Ph.D. thesis, University of Alberta, 1995.
[16] M. A. Quraan, Ph.D. thesis, University of Alberta, 1997.
[17] D. E. Tiller, M.Sc. thesis, University of Saskatchewan, 1995.
[18] G. V. O'Rielly, Ph.D. thesis, University of Melbourne, 1996.
[19] J. M. Vogt *et al.*, Nucl. Instrum. Methods Phys. Res. A **324**, 198 (1993).
[20] G. Mechtersheimer *et al.*, Nucl. Phys. **A324**, 379 (1979).
[21] G. V. O'Rielly, N. R. Kolb, and R. E. Pywell, Nucl. Instrum. Methods Phys. Res. A **368**, 745 (1996).